

# On the nature of the bi-stability jump in the winds of early-type supergiants

Jorick S. Vink<sup>1</sup>, Alex de Koter<sup>2,3</sup>, and Henny J.G.L.M. Lamers<sup>1</sup>

<sup>1</sup> Astronomical Institute, Utrecht University, P.O.Box 80000, NL-3508 TA Utrecht, The Netherlands

<sup>2</sup> Astronomical Institute 'Anton Pannekoek', University of Amsterdam, Kruislaan 403, NL-1098 SJ Amsterdam, The Netherlands

<sup>3</sup> Advanced Computer Concepts, Code 681, Goddard Space Flight Center, Greenbelt, MD 20771, USA

the date of receipt and acceptance should be inserted later

**Abstract.** We study the origin of the bi-stability jump in the terminal velocity of the winds of supergiants near spectral type B1. Observations show that here the ratio  $v_\infty/v_{\text{esc}}$  drops steeply from about 2.6 at types earlier than B1 to a value of  $v_\infty/v_{\text{esc}}=1.3$  at types later than B2. To this purpose, we have calculated wind models and mass-loss rates for early-type supergiants in a  $T_{\text{eff}}$  grid covering the range between  $T_{\text{eff}} = 12\,500$  and  $40\,000$  K. These models show the existence of a jump in mass loss around  $T_{\text{eff}} = 25\,000$  K for normal supergiants, with  $\dot{M}$  increasing by about a factor five from  $T_{\text{eff}} \simeq 27\,500$  to  $22\,500$  K for constant luminosity. The wind efficiency number  $\eta = \dot{M}v_\infty/(L_*/c)$  also increases drastically by a factor of 2 - 3 near that temperature.

We argue that the jump in mass loss is accompanied by a decrease of the ratio  $v_\infty/v_{\text{esc}}$ , which is the observed bi-stability jump in terminal velocity. Using self-consistent models for two values of  $T_{\text{eff}}$ , we have derived  $v_\infty/v_{\text{esc}} = 2.4$  for  $T_{\text{eff}} = 30\,000$  K and  $v_\infty/v_{\text{esc}} = 1.2$  for  $T_{\text{eff}} = 17\,500$  K. This is within 10 percent of the observed values around the jump.

Up to now, a theoretical explanation of the observed bi-stability jump was not yet provided by radiation driven wind theory. To understand the origin of the bi-stability jump, we have investigated the line acceleration for models around the jump in detail. These models demonstrate that  *$\dot{M}$  increases around the bi-stability jump due to an increase in the line acceleration of Fe III below the sonic point*. This shows that the mass-loss rate of B-type supergiants is very sensitive to the abundance and the ionization balance of iron.

Furthermore, we show that the elements C, N and O are important line drivers in the *supersonic* part of the wind. The *subsonic* part of the wind is dominated by the line acceleration due to Fe. Therefore, CNO-processing is expected *not* to have a large impact on  $\dot{M}$  but it might have impact on the terminal velocities.

Finally, we discuss the possible role of the bi-stability jump on the mass loss during typical variations of Luminous Blue Variable stars.

**Key words:** Radiative transfer – Stars: early-type – Stars: mass-loss – Stars: supergiants – Stars: winds

## 1. Introduction

In this paper we investigate the origin and the consequences of the *bi-stability jump* of the stellar winds of early-type stars near spectral type B1. This bi-stability jump is observed as a steep decrease in the terminal velocity of the winds from  $v_\infty \simeq 2.6v_{\text{esc}}$  for supergiants of types earlier than B1 to  $v_\infty \simeq 1.3v_{\text{esc}}$  for supergiants of types later than B1 (Lamers et al. 1995). We will show that this jump in the wind velocity is accompanied by a jump in the mass-loss rate with  $\dot{M}$  increasing by about a factor of five for supergiants with  $T_{\text{eff}}$  between 27 500 and 22 500 K.

The theory of radiation driven winds predicts that the mass-loss rates and terminal velocities of the winds of early-type stars depend smoothly on the stellar parameters, with  $v_\infty \simeq 3v_{\text{esc}}$  and  $\dot{M} \propto L^{1.6}$  (Castor et al. 1975, Abbott 1982, Pauldrach et al. 1986, Kudritzki et al. 1989). This theory has not yet been applied to predict the observed jump in the ratio  $v_\infty/v_{\text{esc}}$  for supergiants near spectral type B1. The change from a fast to a slow wind is called the *bi-stability* jump. If the wind momentum  $\dot{M}v_\infty$  were about constant across the bi-stability jump, it would imply that the mass-loss rate would *increase* steeply by about a factor of two from stars with spectral types earlier than B1 to later than B1. Unfortunately, there are no reliable mass-loss determinations from observations for stars later than spectral type B1.

So far, a physical explanation of the nature of this bi-stability jump has been lacking. In this paper, we attempt to provide such an explanation and we investigate

the change in mass-loss rate that is accompanied by the change in  $v_\infty$ .

The concept of a bi-stability jump was first described by Pauldrach & Puls (1990) in connection to their model calculations of the wind of the Luminous Blue Variable (LBV) star P Cygni ( $T_{\text{eff}} = 19.3$  kK). Their models showed that small perturbations in the basic parameters of this star can either result in a wind with a relatively high mass loss, but low terminal velocity, or in a wind with relatively low  $\dot{M}$ , but high  $v_\infty$ . Their suggestion was that the mechanism is related to the behaviour of the Lyman continuum. If the Lyman continuum exceeds a certain optical depth, then as a consequence, the ionization of the metals shifts to a lower stage. This causes a larger line acceleration  $g_L$  and finally yields a jump in  $\dot{M}$ .

The models of Pauldrach & Puls (1990) for P Cygni show that the wind momentum loss per second,  $\dot{M}v_\infty$ , is about constant on both sides of the jump (see Lamers & Pauldrach 1991). So Lamers et al. (1995) put forward the idea that the mass-loss rate for normal stars could increase by about a factor of two, if  $v_\infty$  decreases by a factor of two, so that  $\dot{M}v_\infty$  is constant on both sides of the jump.

Whether this is indeed the case, is still unknown. To investigate the behaviour of the mass loss at the bi-stability jump, we will derive mass-loss rates for a grid of wind models over a range in  $T_{\text{eff}}$ . The main goal of the paper is to understand the processes that cause the bi-stability jump. Although our results are based on complex numerical simulations, we have attempted to provide a simple picture of the relevant physics. We focus on the observed bi-stability jump for normal supergiants. Nevertheless, these results may also provide valuable insight into the possible bi-stable winds of LBVs.

It is worth mentioning that Lamers & Pauldrach (1991) and Lamers et al. (1999) suggested that the bi-stability mechanism may be responsible for the outflowing disks around rapidly-rotating B[e] stars. Therefore our results may also provide information about the formation of rotation induced bi-stable disks.

The paper is organized in the following way. In Sect. 2 we describe the basic stellar wind theory. In particular we concentrate on the question: “what determines  $\dot{M}$  and  $v_\infty$ ?” We show that  $\dot{M}$  is determined by the radiative acceleration in the *subsonic* region. In Sect. 3 we explain the method that we use to calculate the radiative acceleration with a Monte Carlo technique and the mass-loss rates of a grid of stellar parameters. Sect. 4 describes the properties of the models for which we predict  $\dot{M}$ . In Sect. 5 our predicted bi-stability jump in mass loss will be presented. Then, in Sect. 6 we discuss the origin of this jump and show that it is due to a shift in the ionization balance of Fe IV to Fe III. Then, we discuss the possible role of the bi-stability jump in  $\dot{M}$  on the variability of LBV stars in Sect. 7. Finally, in Sect. 8, the study will be summarized and discussed.

## 2. What determines $\dot{M}$ and $v_\infty$ ?

### 2.1. The theory of $\dot{M}$ determination

Mass loss from early-type stars is due to radiation pressure in lines and in the continuum (mainly by electron scattering). Since the radiative acceleration by line processes is the dominant contributor, the winds are “line-driven”, i.e. the momentum of the radiation is transferred to the ions by line scattering or line absorption. Line-scattering and line absorption occur at all distances in the wind, from the photosphere up to distances of tens of stellar radii. So the radiative acceleration of the wind covers a large range in distance.

The equation of motion of a stationary stellar wind is

$$v \frac{dv}{dr} = -\frac{GM_*}{r^2} - \frac{1}{\rho} \frac{dp}{dr} + g_{\text{rad}}(r) \quad (1)$$

where  $g_{\text{rad}}$  is the radiative acceleration. Together with the mass continuity equation

$$\dot{M} = 4\pi r^2 \rho(r) v(r) \quad (2)$$

and the expression for the gas pressure  $p = \mathcal{R}\rho T/\mu$ , where  $\mathcal{R}$  is the gas constant and  $\mu$  is the mean mass per free particle in units of  $m_H$ , we find the equation of motion

$$v \frac{dv}{dr} = \left\{ \frac{2a^2}{r} - \frac{GM_{\text{eff}}}{r^2} + g_L \right\} / \left\{ 1 - \frac{a^2}{v^2} \right\} \quad (3)$$

where  $a$  is the isothermal speed of sound. For simplicity we have assumed that the atmosphere is isothermal. In this expression the effective mass  $M_{\text{eff}} = M_*(1 - \Gamma_e)$  is corrected for the radiation pressure by electron scattering.  $g_L$  is the line acceleration. The equation has a singularity at the point where  $v(r) = a$ , this critical point is the sonic point. If the line acceleration  $g_L(r)$  is known as a function of  $r$ , the equation can be solved numerically. A smoothly accelerating wind solution requires that the numerator of Eq. 3 reaches zero exactly at the sonic point where the denominator vanishes.

It should be stated that *this* critical point (sonic point) at  $r_c \simeq 1.025R_*$  and  $v_c \simeq 20 \text{ km s}^{-1}$  is *not* the same as the CAK critical point. The CAK critical point is located much further out in the wind at  $r_c \simeq 1.5R_*$  and about  $v_c \simeq 0.5v_\infty$ . If the line acceleration  $g_L$  in Eq. 3 were to be rewritten as a function of velocity gradient instead of radius, then one would find the CAK critical point. Pauldrach et al. (1986) showed that if the finite disk correction to the CAK theory is applied, then the Modified CAK critical point moves inward and is located at  $r_c \simeq 1.04R_*$  and at  $v_c \simeq 100 \text{ km s}^{-1}$ . This is much closer to the sonic point! Although the (Modified) CAK critical solution may well provide the correct mass-loss rate and terminal velocity, there is concern about its physical reality (see e.g. Lucy 1998 and Lamers & Cassinelli 1999 for a thorough discussion). Lucy (1998) has given arguments favouring the

sonic point as the physical more meaningful critical point. We will use the sonic point as the physically relevant critical point. This is the point where the mass-loss rate is fixed. Throughout the paper we will therefore refer to the *subsonic* part of the wind for the region close to the photosphere where the mass loss is determined, and to the *supersonic* part for the region beyond the sonic point where the mass-loss rate is already fixed, but the velocity has still to be determined.

The critical solution can be found by numerically integrating Eq. 3, starting from some lower boundary  $r_0$  in the photosphere, with pre-specified values of  $T_0$  and  $\rho_0$  and with a trial value of  $v_0$ . The value of  $v_0$  that produces a velocity law that passes smoothly through the critical point is the correct value. Alternatively, for a non-isothermal wind with a pre-specified  $T(\tau)$ -relation, one can integrate inwards from the critical point with an assumed location  $r_c$ , and then adjust this value until the inward solution gives a density structure that reaches  $\tau = 2/3$  at the location where  $T(r) = T_{\text{eff}}$  (e.g. see Pauldrach et al. 1986). The critical solution specifies the values of  $r_0 \simeq R_*$ ,  $\rho_0$  (given by  $\tau(r_0) = 2/3$ ) and  $v_0$  at the lower boundary. This fixes the value of  $\dot{M}$  via the mass continuity equation (Eq. 2). Note that  $\dot{M}$  is determined by the conditions in the *subsonic* region!

We will show below that an *increase* in  $g_L(r)$  in the subsonic region results in an *increase* in  $\dot{M}$ . This can be understood because in the *subsonic* region, where the denominator of Eq. 3 is negative, an increase in  $g_L$  gives a smaller velocity gradient. Integrating from the sonic point inwards to the lower boundary with a smaller velocity gradient, implies that the velocity the lower boundary should be higher and hence the mass-loss rate,  $\dot{M} = 4\pi r_0^2 \rho_0 v_0$ , must be higher. On the other hand, an increase in  $g_L$  in the *supersonic* region, yields a larger velocity gradient and this would directly increase the terminal velocity  $v_\infty$ .

Another way to understand how an increase in  $\dot{M}$  is caused by an increase in  $g_L$  below the sonic point, is based on the realization that the density structure of the subsonic region is approximately that of a static atmosphere. This can be seen in Eq. 1. Since the term  $v \, dv/dr$  is much smaller than the acceleration of gravity, it can approximately be set to zero in the subsonic region. (This is not correct close to the sonic point.) In an isothermal static atmosphere the density structure follows the pressure scaleheight. Adding an extra outward force in the subsonic region results in an increase of the pressure-scaleheight and hence in a slower outward decrease in density. This means that just below the sonic point, where  $v \simeq a$ , the density  $\rho$  will be higher than without the extra force. Applying the mass continuity equation (Eq. 2) at the sonic point then shows that the mass-loss rate will be higher than without the extra force in the subsonic region. (See Lamers & Cassinelli 1999 for a thorough discussion).

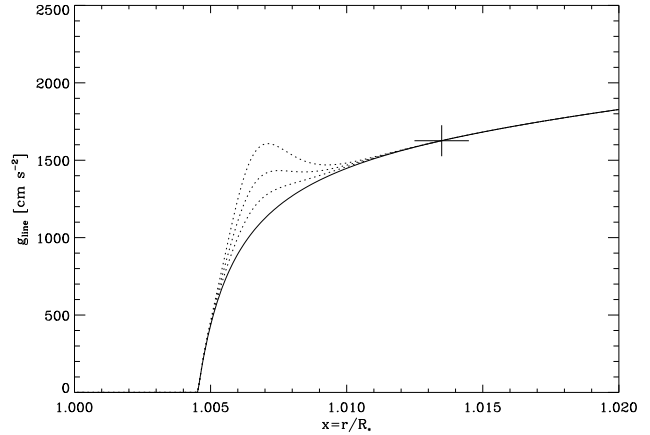


**Fig. 1.** Extra “bumps” on the radiative acceleration  $g_L(r)$  below the sonic point. The solid line is  $g_L(r)$  of the model without a “bump”. The dotted lines show  $g_L(r)$  with the adopted bumps with peakheights of 150, 300 and 500  $\text{cm s}^{-2}$ . The cross indicates the sonic point at  $1.0135 R_*$ .

## 2.2. A simple numerical experiment: the sensitivity of $\dot{M}$ on the subsonic $g_L$

A simple numerical experiment serves to demonstrate the dependence of  $\dot{M}$  on the radiative acceleration in the subsonic region. We start with an isothermal model of the wind from a star of  $M_{\text{eff}} = 20M_\odot$ ,  $R_* = 16.92R_\odot$ ,  $T_{\text{eff}} = 25\,000$  K,  $T_{\text{wind}} = 0.8T_{\text{eff}} = 20\,000$  K. We then specify the line acceleration  $g_L(r)$  in such a way that it produces a stellar wind with a mass-loss rate of  $1.86 \cdot 10^{-7} M_\odot \text{yr}^{-1}$  and with a  $\beta$ -type wind velocity law

$$v(r) = v_\infty \left(1 - \frac{R_*}{r}\right)^\beta \quad (4)$$

where  $\beta = 1$  and  $v_\infty = 1500 \text{ km s}^{-1}$ . (This  $g_L(r)$  is found by solving Eq. 3 with this fixed velocity law). This model is very similar to one of the models near the bi-stability jump that we will calculate in detail in Sect. 5. As a lower boundary we choose the point where  $\rho = 10^{-10} \text{ g cm}^{-3}$  at  $r_0 = R_*$ . Figure 1 shows the resulting variation of  $g_L(r)$ . Adopting this variation of  $g_L(r)$  and solving the momentum equation with the condition that the solution goes smoothly through the sonic point, we retrieve the input mass-loss rate and input velocity law, as one would expect. The sonic point is located at  $r_c = 1.0135R_*$  where  $v = 16.6 \text{ km s}^{-1}$ , and where  $g_L(r) = 1.63 \cdot 10^3 \text{ cm s}^{-2}$ .

Let us study what happens to  $\dot{M}$  and  $v_\infty$  if we change the line acceleration in the subsonic region. To this purpose we add a Gaussian “bump” to  $g_L(r)$ . This bump is characterized by

$$g_L^{\text{bump}}(r) = g_L^{\text{peak}} \exp \left\{ -\left( \frac{z - z_p}{\Delta z} \right)^2 \right\} \quad (5)$$

where  $z = 1/\{(r/R_*) - 1\}$ ,  $z_p = 150$  describes the location of the peak at  $r/R_* = 1.0067$  and  $\Delta z = 30$  gives the width

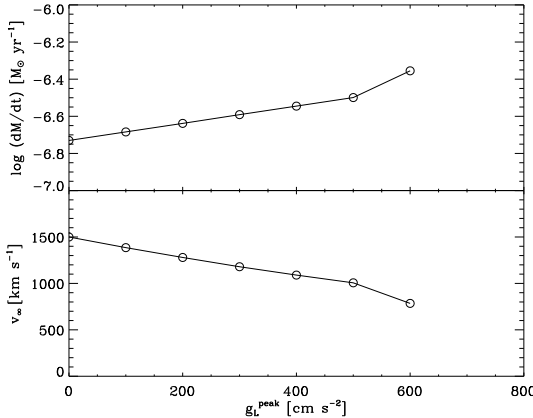


**Fig. 2.** The effect of increasing the line acceleration in the subsonic region on  $\dot{M}$  (upper panel) and a simple derivation of its effect on  $v_\infty$  (lower panel). The horizontal axis gives the peak-value,  $g_L^{\text{peak}}$ , of the bump in  $g_L(r)$  in the subsonic region (i.e. the bumps in Fig. 1).

of the bump ( $\Delta r \simeq 0.0015R_*$ ). The line acceleration with the extra bumps is shown in Fig. 1.

The solution of the momentum equation, with the condition that it passes smoothly through the sonic point, gives the velocity at the lower boundary and hence the mass-loss rate. The upper panel of Fig. 2 shows the resulting mass-loss rates as a function of the peak value of the bump in the line acceleration in the subsonic region. We see that as the line acceleration in the subsonic region increases,  $\dot{M}$  increases.

### 2.3. The effect of an increased $\dot{M}$ on $v_\infty$

Once  $\dot{M}$  is fixed by the processes in the subsonic region, the radiative acceleration in the supersonic region then determines the terminal velocity  $v_\infty$  that the wind will reach. This can easily be seen in the following way. Integrating the momentum equation (Eq. 1) in the supersonic region from the critical point  $r_c$  to infinity, and ignoring the influence of the gas pressure, gives

$$\int_{r_c}^{\infty} g_L(r) dr = \frac{1}{2} v_{\text{esc}}^2 + \frac{1}{2} v_\infty^2 \quad (6)$$

so

$$v_\infty^2 \simeq 2 \int_{r_c}^{\infty} g_L(r) dr - v_{\text{esc}}^2 \quad (7)$$

Here we have used the observed property that  $v_\infty \gg a$  and that  $r_c - r_0 \ll R_*$ , so  $r_c \simeq R_*$ . Eq. 7 says that  $v_\infty$  is determined by the integral of  $g_L(r)$  in the supersonic region.

The radiative acceleration in the supersonic part of the wind will decrease as  $\dot{M}$  is forced to increase by an increase in the radiative acceleration in the subsonic part of the

wind. This is because the optical depth of the optically thick driving lines, which is proportional to the density in the wind, will increase. Thus an increase in  $\dot{M}$  results in an increase of the line optical depth. This results in a decrease of  $g_L$  in the supersonic region, which gives a lower terminal velocity  $v_\infty$ . We will estimate this effect below.

Assume that the radiative acceleration by lines depends on the optical depth in the wind, as given by CAK theory (Castor et al. 1975).

$$g_L(r) = g_e M(t) = \frac{\sigma_e L_*}{4\pi r^2 c} k t^{-\alpha} \quad (8)$$

where  $k$  and  $\alpha$  are constants and  $g_e$  is a reference value describing the acceleration due to electron scattering. It is given by  $g_e = \frac{\sigma_e L_*}{4\pi r^2 c}$ . The optical depth parameter is

$$t = \sigma_e v_{\text{th}} \rho (dr/dv) \quad (9)$$

where  $v_{\text{th}}$  is the mean thermal velocity of the protons. Let us define  $g_L^{\text{init}}(r)$  as the radiative acceleration in the supersonic part of the initial wind model, i.e. without the increased mass-loss rate due to the bump in the subsonic region, and  $g_L(r)$  as the radiative acceleration of the model with the increased  $\dot{M}$ . From Eqs. 8 and 9 with Eq. 2 we find that

$$g_L(r) = g_L^{\text{init}} \left\{ \frac{r^2 v dv / dr}{(r^2 v dv / dr)^{\text{init}}} \right\}^\alpha \left\{ \frac{\dot{M}^{\text{init}}}{\dot{M}} \right\}^\alpha \quad (10)$$

where the superscript “init” refers to the initial model.

Let us now compare the terminal velocities of the initial model without the bump, to that with the increased mass-loss rate due to the bump, in a simple but crude way, by solving the momentum equation in the supersonic part of the wind. If we neglect the terms due to the gas pressure and due to the gravity, the momentum equation in the supersonic part of the wind reduces to

$$v \frac{dv}{dr} \simeq g_L(r) \quad (11)$$

Solving the equation for the initial model and the model with the increased  $\dot{M}$  results in the following expression

$$v \frac{dv}{dr} \simeq \left\{ v \frac{dv}{dr} \right\}^{\text{init}} \left\{ \frac{\dot{M}^{\text{init}}}{\dot{M}} \right\}^{\alpha/(\alpha-1)} \quad (12)$$

So the ratio between the terminal velocities of the models with and without the increased mass-loss rate is

$$\frac{v_\infty}{v_\infty^{\text{init}}} \simeq \left\{ \frac{\dot{M}^{\text{init}}}{\dot{M}} \right\}^{\alpha/(2-2\alpha)} \simeq \left\{ \frac{\dot{M}}{\dot{M}^{\text{init}}} \right\}^{-3/4} \quad (13)$$

where we adopted  $\alpha = 0.60$  (Pauldrach et al. 1986) for the last expression. We see that  $v_\infty$  will decrease roughly as  $\dot{M}^{-3/4}$  when the mass-loss rate increases. The result is shown in the lower panel of Fig. 2.

We realize that this numerical test is a drastic simplification of the real situation: (a) we have assumed an isothermal wind; (b) we have taken the lower boundary at a fixed density; (c) we have ignored possible changes in the ionization of the wind due to changes in  $\dot{M}$  and (d) we have ignored the role of the gas pressure and of gravity in estimating the change in  $v_\infty$ . However, this simple test serves the purpose of explaining *qualitatively* that the mass-loss rate depends on the radiative acceleration in the subsonic part of the wind only, and that an increase in the mass-loss rate due to an increase of  $g_L$  in the subsonic region will also be accompanied by a decrease in  $v_\infty$ . In the rest of the paper, we will *quantitatively* calculate radiative accelerations and mass-loss rates with a method which will be described in Sect. 3.

Thus, an *increase* in the radiative acceleration in the *subsonic* region of the wind results in an *increase* of  $\dot{M}$  and a *decrease* in  $v_\infty$ . So, in order to understand the origin of the bi-stability jump of radiation driven winds, and to predict its effect on  $\dot{M}$  and  $v_\infty$ , we should pay close attention to the calculated radiative acceleration in the *subsonic* part of the wind.

### 3. The method to predict $\dot{M}$

In order to understand the nature of the bi-stability jump, we calculate a series of radiation driven wind models for supergiants in the range of  $T_{\text{eff}} = 12\,500$  to  $40\,000$  K. The calculation of the radiative acceleration of the winds requires the computation of the contributions of a very large number of spectral lines. To this end, we first calculate the thermal, density and ionization structure of a wind model computed with the non-LTE expanding atmosphere code ISA-WIND (de Koter et al. 1993)(for details, see Sect. 4). We then calculate the radiative acceleration by following the fate of a very large number of photons that are released from below the photosphere into the wind, by means of a Monte Carlo technique. In this section, we describe the basic physical properties of the adopted Monte Carlo (MC) technique which was first applied to the study of winds of early-type stars by Abbott & Lucy (1985). Then, we describe the calculation of the radiative acceleration by lines with the MC method, and finally the method for calculating theoretical mass-loss rates.

#### 3.1. Momentum transfer by line scattering

The lines in the MC method are described in the Sobolev approximation. This approximation for the line acceleration is valid if the physical conditions over a Sobolev length do not change significantly, i.e.

$$\frac{1}{f} \left| \frac{df}{dr} \right| \ll \frac{1}{v_t} \left| \frac{dv}{dr} \right| \quad (14)$$

where  $f$  is any physically relevant variable for the line driving, e.g. density, temperature or ionization fraction.  $v_t$  is

a combination of thermal and turbulent velocities. Eq. 14 shows that the validity range of the Sobolev approximation is in practice somewhat arbitrary, since it depends on the value of the turbulent velocity which is poorly known. Nevertheless, the Sobolev approximation is often used (e.g. Abbott & Lucy 1985) and we will also adopt it in calculating the line acceleration and mass loss, mainly because of computational limitations. We cannot exclude that due to the use of the Sobolev approximation we may predict quantitatively inaccurate line accelerations below the sonic point. However, if an exact treatment would be followed, then this is expected to have a systematic effect on the line acceleration for *all* models. Therefore, we do not expect our conclusions regarding the origin of the bi-stability jump to be affected.

The Sobolev approximation implies that for scatterings in the frame co-moving with the ions in the wind (co-moving frame, CMF), the incident and emerging frequencies are both equal to the rest frequency of the line transition  $\nu_0$  in the CMF.

$$\nu'_{\text{in}} = \nu_0 = \nu'_{\text{out}} \quad (15)$$

where  $\nu'_{\text{in}}$  and  $\nu'_{\text{out}}$  are the incident and emerging frequencies in the CMF. In terms of quantities seen by an outside observer, these two CMF frequencies are given by:

$$\nu'_{\text{in}} = \nu_{\text{in}} \left( 1 - \frac{\mu_{\text{in}} v}{c} \right) \quad (16)$$

and

$$\nu'_{\text{out}} = \nu_{\text{out}} \left( 1 - \frac{\mu_{\text{out}} v}{c} \right) \quad (17)$$

where  $\nu_{\text{in}}$  and  $\nu_{\text{out}}$  are the incident and emergent frequencies for an outside observer;  $\mu_{\text{in}}$  and  $\mu_{\text{out}}$  are the direction cosines with respect to the radial flow velocity of the photons at the scattering point and  $v$  is the radial flow velocity of the scattering ion for an outside observer. Thermal motions of the scattering ions are assumed to be negligible compared to the motion of the outward flow. Note that we adopted the same velocity  $v$  for the ion before and after the photon interaction (Eqs. 16 and 17). This is justified since the change in velocity due to the transfer of momentum from a photon to an ion is very small, i.e. about  $10^1$  cm s $^{-1}$  per scattering.. Therefore, the change in  $\nu_{\text{in}}$  and  $\nu_{\text{out}}$  is mainly determined by a change in direction angle.

Combining Eqs. 16 and 17 gives the conservation of co-moving frequency in a scattering event (Abbott & Lucy 1985).

$$\nu_{\text{in}} \left( 1 - \frac{\mu_{\text{in}} v}{c} \right) = \nu_{\text{out}} \left( 1 - \frac{\mu_{\text{out}} v}{c} \right) \quad (18)$$

Because the energy and momentum of a photon are  $E = h\nu$  and  $p = h\nu/c$ , the equation can be rewritten in the following way:

$$p_{\text{in}} \mu_{\text{in}} - p_{\text{out}} \mu_{\text{out}} = \frac{E_{\text{in}} - E_{\text{out}}}{v} \quad (19)$$

Eq. 19 links the change in radial *momentum* of a photon in an interaction with an ion with velocity  $v$  to the *energy* loss of the photon. In order to determine the line acceleration  $g_L$  we will need to derive the momentum transfer from the photons to the *ions* in the wind.

For an outside observer, the conservation of radial momentum is:

$$mv_1 + \frac{h\nu_{\text{in}}}{c} \mu_{\text{in}} = mv_2 + \frac{h\nu_{\text{out}}}{c} \mu_{\text{out}} \quad (20)$$

where  $m$  is the mass of the moving ion and  $v_1$  and  $v_2$  are the radial velocities of the ion just before and after the scattering. For an outside observer:

$$\nu_{\text{in}} = \nu_0 (1 + \frac{\mu_{\text{in}} v}{c}) \quad (21)$$

and

$$\nu_{\text{out}} = \nu_0 (1 + \frac{\mu_{\text{out}} v}{c}) \quad (22)$$

Again, the change in frequency is dominated by the change in direction angle. So the change in radial velocity per scattering,  $\Delta v = v_2 - v_1$ , is small compared to  $v$  and is given by

$$\begin{aligned} \Delta v &= v_2 - v_1 \\ &= \frac{h\nu_0}{mc} (1 + \frac{\mu_{\text{in}} v}{c}) \mu_{\text{in}} - \frac{h\nu_0}{mc} (1 + \frac{\mu_{\text{out}} v}{c}) \mu_{\text{out}} \end{aligned} \quad (23)$$

Since  $v \ll c$ , Eq. 23 becomes

$$\Delta v = v_2 - v_1 = \frac{h\nu_0}{mc} (\mu_{\text{in}} - \mu_{\text{out}}) \quad (24)$$

This relation describes the velocity increase of the ion depending on the directions  $\mu_{\text{in}}$  and  $\mu_{\text{out}}$  of the photon. In case  $\mu_{\text{in}} = \mu_{\text{out}}$  then  $\Delta v = 0$ , as one would expect. The increase in the radial momentum  $\Delta p = m \Delta v$  of the scattering ion is now given by:

$$\begin{aligned} \Delta p = m(v_2 - v_1) &= \frac{h\nu_0}{c} (\mu_{\text{in}} - \mu_{\text{out}}) \\ &= \frac{h\nu_{\text{in}} - h\nu_{\text{out}}}{v} = \frac{\Delta E}{v} \end{aligned} \quad (25)$$

where  $\Delta E = E_{\text{in}} - E_{\text{out}}$  is the loss of *radiative* energy. This equation shows that the increase in the momentum of the *ions* can be calculated from the loss of energy of the *photons* when these are followed in their path through the wind by means of the Monte Carlo method.

Multiplying both sides of Eq. 25 by  $v$  and using the fact that for each scattering  $v_2 \simeq v_1$  so  $v \simeq (v_1 + v_2)/2$ , gives:

$$\frac{1}{2} m(v_2^2 - v_1^2) = h\nu_{\text{in}} - h\nu_{\text{out}} \quad (26)$$

Equation 26 says that the gain of kinetic energy of the ions in the radial direction equals the energy loss of the photons.

### 3.2. Scattering and absorption processes in the MC calculations

The radiative acceleration as a function of distance is calculated by means of the MC technique by following the fate of the photons using the program MC-WIND (de Koter et al. 1997). In the calculation of the path of the photons we have properly taken into account the possibility that the photons can be scattered or absorbed & re-emitted due to true absorption or eliminated because they are scattered back into the star.

The radiative transfer in MC-WIND is calculated in the Sobolev approximation. Multiple line and continuum processes are included in the code. The continuum processes included are electron scattering and thermal absorption and emission. The line processes included are photon scattering and photon destruction by collisional de-excitation. In deciding whether a continuum or a line event takes place, we have improved the code in the following way: The key point of the Monte-Carlo “game” is that *line* processes can only occur at specific points in each shell of the stellar wind, whereas *continuum* processes can occur at any point. The correct way of treating the line and continuum processes is by comparing a random optical depth value to the *combined* optical depth for line and continuum processes along the photon’s path. First, this combined optical depth is compared to a random number to decide whether a continuum or a line process takes place. This first part of the treatment is basically the same as described by Mazzali & Lucy (1993) for the case of line and electron scatterings only. Now, after it has been decided that the process will be a continuum process, a second random number is drawn to decide *which* continuum process will take place, an electron scattering or absorption.

### 3.3. The calculation of the radiative acceleration $g_L(r)$

The radiative acceleration of the wind was calculated by following the fate of the photons emitted from below the photosphere with the MC technique. To this purpose the atmosphere is divided into a large number of concentric, thin shells with radius  $r$ , thickness  $\Delta r$  containing a mass  $\Delta m(r)$ .

The loss of photon energy due to all scatterings that occur within each shell are calculated to retrieve the total line acceleration  $g_L(r)$  per shell. The total line acceleration per shell summed over all line scatterings in that shell equals

$$g_L(r) = \frac{1}{\Delta m(r)} \frac{\sum \Delta p(r)}{\Delta t} \quad (27)$$

where  $p(r)$  is the momentum of the ions in the shell. The momentum gained by the ions in the shell is equal to the momentum lost by the photons due to interactions in that shell. Using the relationship between  $\Delta m(r)$  and  $\Delta r$  for

thin concentric shells,  $\Delta m(r) = 4\pi r^2 \rho(r) \Delta r$ , and the derived relation between momentum and energy transfer of the photons  $\Delta p = \Delta E/v$  (Eq. 25),  $g_L(r)$  can be rewritten as

$$g_L(r) = \frac{1}{4\pi r^2 \rho(r) \Delta r} \frac{\Sigma \Delta E(r)}{v(r) \Delta t} \quad (28)$$

where  $\Sigma \Delta E(r)$  is sum of the energy loss of all the photons that are scattered in the shell. Now using mass continuity (Eq. 2) and the fact that the total energy transfer  $\Sigma \Delta E(r)$  divided by the time interval  $\Delta t$  equals the rate at which the radiation field loses energy,  $-\Delta L(r)$ , i.e.  $\Sigma \Delta E(r)/\Delta t = -\Delta L(r)$ , the expression for  $g_L(r)$ , which is valid for each shell, simply becomes (Abbott & Lucy 1985)

$$g_L(r) = - \frac{1}{\dot{M}} \frac{\Delta L(r)}{\Delta r} \quad (29)$$

The line list that is used for the MC calculations consists of over  $10^5$  of the strongest lines of the elements H - Zn from a line list constructed by Kurucz(1988). Lines in the wavelength region between 50 and 7000 Å are included in the calculations with ionization stages up to stage VI. Typically about  $2 \cdot 10^5$  photon packets, distributed over the spectrum at the lower boundary of the atmosphere were followed for each model, i.e. for each adopted set of stellar and wind parameters. For several more detailed models we calculated the fate of  $2 \cdot 10^7$  photon packets. The wind was divided in about 50-60 concentric shells, with many narrow shells in the subsonic region and wider shells in supersonic layers. The division in shells is essentially made on the basis of a Rosseland optical depth scale. Typical changes in the logarithm of this optical depth are about 0.13.

### 3.4. The determination of $\dot{M}$

We predict the mass-loss rates for a grid of model atmospheres to study the behaviour of  $\dot{M}$  near the bi-stability jump. For a given set of stellar parameters we calculate the mass loss in the following way:

1. For fixed values of  $L$ ,  $T_{\text{eff}}$ ,  $R_*$  and  $M_{\text{eff}}$  we adopt several values of the input mass loss  $\dot{M}^{\text{inp}}$  (within reasonable bounds predicted by CAK theory).
2. For each model we adopt a wind with a terminal velocity of 1.3, 2.0 or 2.6 times the effective escape velocity, given by

$$v_{\text{esc}} = \sqrt{\frac{2GM_{\text{eff}}}{R_*}} \quad (30)$$

A  $\beta$ -type velocity law with  $\beta = 1$  was adopted, appropriate for OB stars (Groenewegen & Lamers 1989; Puls et al. 1996)

3. For each set of stellar and wind parameters we calculate a model atmosphere with ISA-WIND (see Sect. 4). This code gives the thermal structure, the ionization and excitation structure and the population of the energy levels of all relevant ions.
4. For each model the radiative acceleration was calculated with the MC-WIND program that uses the Monte Carlo method described above.
5. For each set of stellar parameters and for each adopted value of  $v_\infty$  we check which one of the adopted mass-loss rates is consistent with the radiative acceleration. This consistency was checked in the following way: Neglecting the term due to the gas pressure, one can write the equation of motion in the following way:

$$v \frac{dv}{dr} = - \frac{GM_{\text{eff}}}{r^2} + g_L(r) \quad (31)$$

Using the expression for the line acceleration (Eq. 29) and integrating the equation of motion (Eq. 31) from the stellar surface to infinity gives

$$\frac{1}{2} \dot{M} (v_\infty^2 + v_{\text{esc}}^2) = \Delta L = \dot{M} \int_{R_*}^{\infty} g_L(r) dr \quad (32)$$

$\Delta L = \Sigma \Delta L(r)$ , is the total amount of radiative energy, summed over all the shells, that is lost in the process of line-interaction and is transferred into kinetic energy of the ions as given in Eq. 26. Equation 32 states that the momentum transferred from the radiation into the wind is used to lift the mass loss out of the potential well and to accelerate the wind to  $v_\infty$ . Only *one* value of  $\dot{M}$  will satisfy this equation (Lucy & Abbott 1993). This is the predicted mass-loss rate.

We note that Eq. 32 only describes the “global” consistency of the mass-loss rate with the radiative acceleration. For the set-up of the model atmosphere the velocity law  $v(r)$  is needed as input. This means that although the  $\dot{M}$  calculation is globally consistent in terms of kinetic wind energy, the velocity is not necessarily locally consistent, since the equation of motion is not solved. Instead, we have used observed values for  $v_\infty$  and  $\beta$  for the velocity law. Since the total amount of radiative energy in Eq. 32 is mainly determined in the *supersonic* region, where the Sobolev approximation is an excellent approximation,  $\Delta L$  is accurately calculated. This implies that if one adopts the correct values for the terminal velocity, one may predict accurate values for  $\dot{M}$ !

## 4. The model atmospheres

The calculation of the mass-loss rates by the method described in the previous section requires the input of a model atmosphere, before the radiative acceleration and  $\dot{M}$  can be calculated.

The model atmospheres used for this study are calculated with the most recent version of the non-LTE unified

Improved Sobolev Approximation code ISA-WIND for stars with extended atmospheres. For a detailed description of this code we refer to de Koter et al. (1993, 1997). Here, we just make a few relevant remarks.

ISA-WIND treats the atmosphere in a unified manner, i.e. no artificial separation between photosphere and wind is assumed. This is distinct from the so-called “core-halo” approaches. In the photosphere the density structure follows from a solution of the momentum equation taking into account gas and radiative pressure on electrons. The velocity law follows from this density structure via the mass continuity equation. Near the sonic point, a smooth transition is made to a  $\beta$ -type velocity law for the supersonic part of the wind (see Eq. 4).

The temperature structure in the wind is computed under the assumption of radiative equilibrium in an extended grey LTE atmosphere. The temperature in the wind is not allowed to drop below a certain minimum value  $T_{\min} = 1/2 T_{\text{eff}}$  (Drew 1989). Finally, the chemical species included explicitly in the non-LTE calculations are H, He, C, N, O and Si. The complexity of the model atoms is similar to that used by de Koter et al. (1997). For the iron-group elements, which are important for the radiative acceleration, we calculate the ionization/excitation equilibrium in the *modified nebular approximation* (see Schmutz 1991). In this representation the ionization equilibrium is given by

$$\frac{N_{j+1}n_e}{N_j} = \{(1-\zeta)W + \zeta\}W \left(\frac{T_e}{T_R}\right)^{1/2} \left(\frac{N_{j+1}n_e}{N_j}\right)_{T_R}^{\text{LTE}} \quad (33)$$

where  $n_e$  and  $T_e$  are the electron density and temperature,  $N_j$  and  $N_{j+1}$  are the ion population numbers,  $T_R = T_R(r, j)$  is the radiation temperature of ion  $j$  at radial depth  $r$ , and  $W$  is a geometrical dilution factor as defined by Schmutz et al. (1990). The last factor of Eq. 33 is the LTE ionization ratio for a temperature  $T_R(r, j)$ . The parameter  $\zeta$ , introduced by Abbott & Lucy (1985), represents the fraction of recombinations going directly to the ground state. The values of  $T_R(r, j)$  are obtained by inverting the above equation, using all 19 ionization ratios available from the ISA-WIND calculation. The radiation temperature of an explicit ion is used that has its ionization potential closest (but lower) to that of the metal ion of interest. For instance, the N II/III ratio is used to define the ionization equilibrium of Fe III/IV.

The excitation state of metastable levels is assumed to be in LTE relative to the ground state. For all other levels we adopt “diluted” LTE populations, defined by

$$\frac{n_u}{n_l} = W \left(\frac{n_u}{n_l}\right)_{T_R}^{\text{LTE}}. \quad (34)$$

where  $n_u$  and  $n_l$  are the excitation population numbers for the upper and lower levels. Clearly, the simplified treatment of the iron-group metals is prompted by the computationally intensive nature of the problem at hand. It

needs to be improved in the future, but we do not expect that our conclusions regarding the nature of the bi-stability jump would be affected. (We return to this in the discussion in Sect. 8).

## 5. The predicted bi-stability jump

Using the procedure as described in Sect. 3.4, we calculated mass-loss rates for stars with a luminosity of  $L_* = 10^5 L_\odot$  and a mass of  $M_* = 20M_\odot$ . The models have effective temperatures between 12 500 and 40 000 K with a stepsize of 2500 K. These parameters are approximately those of OB supergiants, for which Lamers et al. (1995) found the bi-stability in  $v_\infty$ .

We calculated  $\dot{M}$  for wind models with a  $\beta$ -type velocity law with  $\beta = 1$  (Eq. 4) for three values of the  $v_\infty/v_{\text{esc}} = 2.6, 2.0$  and  $1.3$ . Lamers et al. (1995) found that  $v_\infty/v_{\text{esc}} \simeq 2.6$  for stars of types earlier than B1, and  $v_\infty/v_{\text{esc}} \simeq 1.3$  for stars of types later than B2. For the determination of  $v_{\text{esc}}$  we used the effective mass  $M_{\text{eff}} = 17.4 M_\odot$ , with  $\Gamma_e = 0.130$ .

The stellar parameters for the calculated grid are indicated in Table 1. The models are calculated for solar metallicities.

### 5.1. The predicted bi-stability jump in $\dot{M}$

The results are listed in Table 1. This Table gives the values of  $T_{\text{eff}}$ ,  $R_*$ ,  $v_{\text{esc}}$  and  $\dot{M}$  for each temperature and for the three values of  $v_\infty/v_{\text{esc}}$ . We also give the value of the wind efficiency factor  $\eta$ , which describes the fraction of the *momentum* of the radiation that is transferred to the ions

$$\dot{M}v_\infty = \eta \left(\frac{L_*}{c}\right) \quad (35)$$

The fraction of the photon *energy* that is transferred into kinetic energy of the ions is also listed (in column 8). The values for this *energy* efficiency number  $\Delta L/L$  are a factor of about  $10^{-3}$  smaller than the wind *momentum* efficiency number  $\eta$ , which is given in column (7). This is because a photon transfers a large fraction of its momentum during a scattering, but only a very small fraction (of order  $v/c$ ) of its energy. The last column of Table 1 marks three models that will be discussed in more detail in Sect. 6.

The results are plotted in Fig. 3. For each of the three values of  $v_\infty/v_{\text{esc}}$  the value of  $\dot{M}$  is decreasing for decreasing  $T_{\text{eff}}$  between 40 000 and 30 000 K and also between 22 500 and 12 500 K. Between about  $T_{\text{eff}} = 27 500$  K and  $T_{\text{eff}} = 20 000$  K (slightly dependent on  $v_\infty/v_{\text{esc}}$ ) the mass loss *increases* with decreasing  $T_{\text{eff}}$ . These increments in  $\dot{M}$  roughly coincide in  $T_{\text{eff}}$  with the observed bi-stability jump in  $v_\infty/v_{\text{esc}}$  near spectral type B1, at about 21 000 K. For the ratio of  $v_\infty/v_{\text{esc}} = 2.6$ , the increase in  $\dot{M}$  between model A and B equals 45 %. We know from the observations that  $v_\infty/v_{\text{esc}}$  jumps from 2.6 at the hot side

**Table 1.** Stellar parameters of the grid of calculated models.

$\log L/L_\odot = 5.0$ ,  $M = 20M_\odot$ ,  $\Gamma_e = 0.130$ ,  $M_{\text{eff}} = 17.4 M_\odot$ ,  $\beta = 1$ , solar metallicity.

$v_\infty/v_{\text{esc}}$	$T_{\text{eff}}$	$R_*$	$v_{\text{esc}}$	$v_\infty$	$\log \dot{M}$	$\eta$	$\Delta L/L$	model
	(K)	( $R_\odot$ )	(km s $^{-1}$ )	(km s $^{-1}$ )	( $M_\odot/\text{yr}$ )		(in 10 $^{-3}$ )	
1.3	12 500	67.7	310	410	- 6.32	0.095	0.103	C
	15 000	47.0	380	490	- 6.39	0.097	0.126	
	17 500	34.5	440	570	- 6.28	0.146	0.221	
	20 000	26.4	500	650	- 6.22	0.192	0.332	
	22 500	20.9	560	730	- 6.15	0.254	0.493	
	25 000	16.9	630	810	- 6.12	0.302	0.653	
	27 500	14.0	690	900	- 6.40	0.174	0.414	
	30 000	11.8	750	980	- 6.58	0.126	0.326	
	32 500	10.0	810	1060	- 6.58	0.136	0.382	
	35 000	8.6	880	1140	- 6.43	0.207	0.626	
	37 500	7.6	940	1220	- 6.37	0.255	0.826	
	40 000	6.6	1000	1300	- 6.26	0.350	1.210	
	2.0	12 500	67.7	310	630	- 6.74	0.056	0.073
		15 000	47.0	380	750	- 6.62	0.088	0.138
		17 500	34.5	440	880	- 6.49	0.139	0.254
		20 000	26.4	500	1000	- 6.41	0.191	0.398
		22 500	20.9	560	1130	- 6.32	0.264	0.620
		25 000	16.9	630	1250	- 6.48	0.203	0.530
		27 500	14.0	690	1380	- 6.73	0.125	0.360
		30 000	11.8	750	1500	- 6.76	0.128	0.400
		32 500	10.0	810	1630	- 6.71	0.155	0.527
		35 000	8.6	880	1750	- 6.59	0.220	0.801
		37 500	7.6	940	1880	- 6.57	0.247	0.969
		40 000	6.6	1000	2000	- 6.48	0.325	1.356
	2.6	12 500	67.7	310	810	- 6.95	0.045	0.070
		15 000	47.0	380	980	- 6.85	0.067	0.126
		17 500	34.5	440	1140	- 6.69	0.114	0.248
		20 000	26.4	500	1300	- 6.54	0.184	0.458
		22 500	20.9	560	1460	- 6.59	0.184	0.517
		25 000	16.9	630	1630	- 6.79	0.129	0.403
		27 500	14.0	690	1790	- 6.95	0.098	0.337
		30 000	11.8	750	1950	- 6.92	0.115	0.430
		32 500	10.0	810	2120	- 6.86	0.143	0.579
		35 000	8.6	880	2280	- 6.76	0.194	0.845
		37 500	7.6	940	2440	- 6.71	0.233	1.089
		40 000	6.6	1000	2600	- 6.68	0.266	1.327

of 21 000 K to 1.3 at the cool side of 21 000 K (Lamers et al. 1995). Including this observed jump in  $v_\infty/v_{\text{esc}}$  in the mass-loss predictions, provides an even steeper increase in  $\dot{M}$  from models A and B to the smaller value of  $v_\infty/v_{\text{esc}} = 1.3$ , as is shown in the lower part of Fig. 3. This figure shows an increase in  $\dot{M}$  of about a factor of five between  $T_{\text{eff}} = 27\,500$  and 20 000 K. This is our prediction for a bi-stability jump in  $\dot{M}$ .

The exact position of  $T_{\text{eff}}$  of the bi-stability jump in Fig. 3 is somewhat ambiguous, since  $v_\infty$  is adopted from observations, and does not directly follow from our models. For a discussion on the exact position of the jump in  $T_{\text{eff}}$ , see Sect. 8.

To test the sensitivity of our predictions of mass-loss rates for different shapes of the velocity law, we calculated

another series of models with  $\beta = 1.5$ . Since the differences are only about 10 %, we conclude that the predicted mass-loss rates are only marginally sensitive to the *shape* of the adopted velocity law.

## 5.2. The predicted bi-stability jump in $\eta$

Another view at these results can be obtained by plotting the wind efficiency factor  $\eta$ . Figure 4 shows the behaviour of  $\eta$  as a function of  $T_{\text{eff}}$  for the same grid of models as was presented for the mass-loss rates in the upper panel of Fig. 3.

Fig. 4 clearly shows that  $\eta$  is not a constant function of  $T_{\text{eff}}$ . The overall picture shows that for the three values of  $v_\infty/v_{\text{esc}}$ ,  $\eta$  decreases as  $T_{\text{eff}}$  decreases. This is

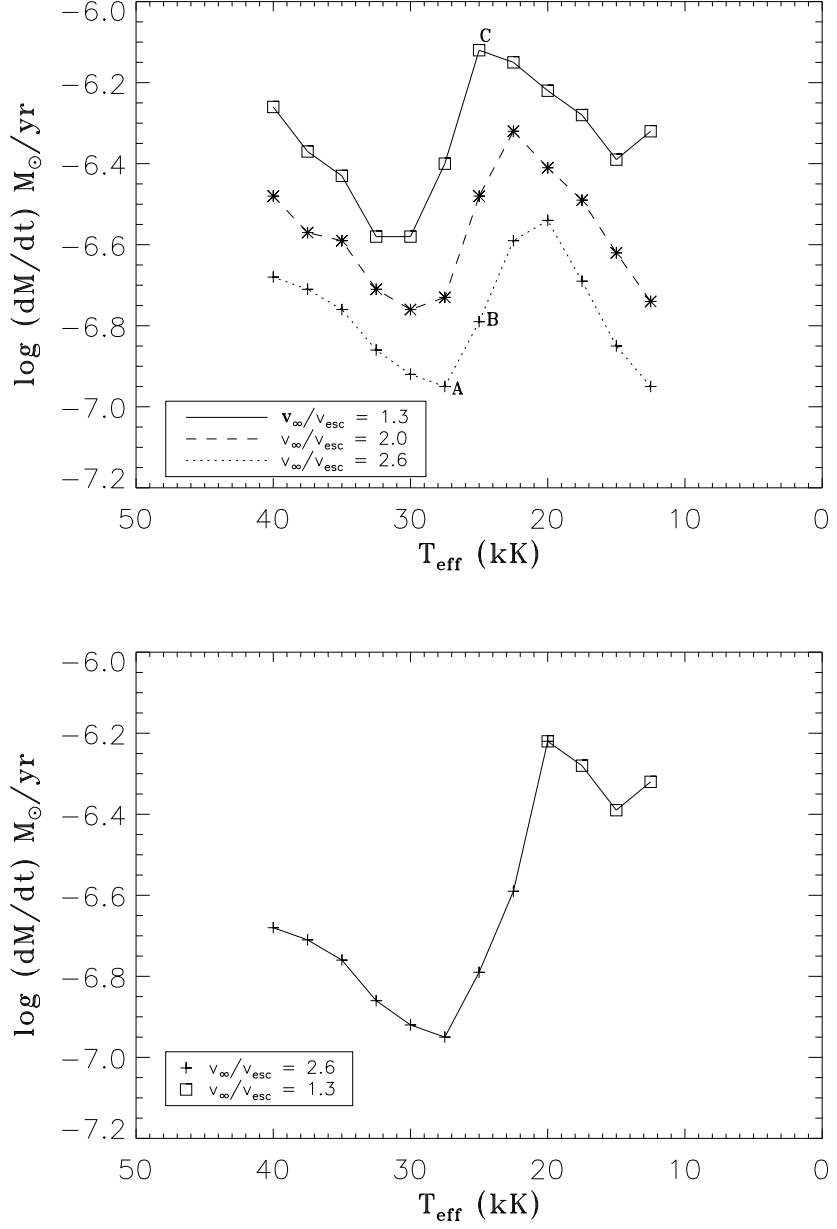


**Fig. 3.** Upper panel: The calculated mass-loss rates  $\dot{M}$  as a function of  $T_{\text{eff}}$  for three values of the ratio  $v_{\infty}/v_{\text{esc}}$ . The values for  $v_{\infty}/v_{\text{esc}}$  are indicated in the lower left corner. The stellar parameters are  $\log L/L_{\odot} = 5.0$ ,  $M = 20 M_{\odot}$  and  $\beta = 1.0$ ; all models are calculated for solar metallicities. Lower panel: The predicted bi-stability jump in  $\dot{M}$  from models with the observed ratios of  $v_{\infty}/v_{\text{esc}} = 2.6$  for  $T_{\text{eff}} > 21,000$  K and  $v_{\infty}/v_{\text{esc}} = 1.3$  for  $T_{\text{eff}} < 21,000$  K, as indicated in the lower left corner.

probably due to the fact that the maximum of the flux distribution shifts to longer wavelengths. At  $\lambda > 1800$  Å there are significantly less lines than at  $\lambda < 1800$  Å. Therefore, radiative acceleration becomes less effective at lower  $T_{\text{eff}}$ . In the ranges of  $40,000 < T_{\text{eff}} < 30,000$  and  $20,000 < T_{\text{eff}} < 12,500$  K,  $\eta$  is almost independent of the adopted value for  $v_{\infty}/v_{\text{esc}}$ . This means that the behaviour

of  $\eta$  is intrinsically present in the model calculations and does not depend on the values adopted for  $v_{\infty}/v_{\text{esc}}$ .

In the range of  $30,000 < T_{\text{eff}} < 20,000$  K, the situation is reversed.  $\eta$  now *increases* by a factor of 2 to 3. This means that the wind momentum loss,  $\dot{M}v_{\infty}$  is *not* constant over the jump, but instead, jumps by a factor of 2 - 3 also. Since  $v_{\infty}$  drops by a factor of about two,  $\dot{M}$  is expected to

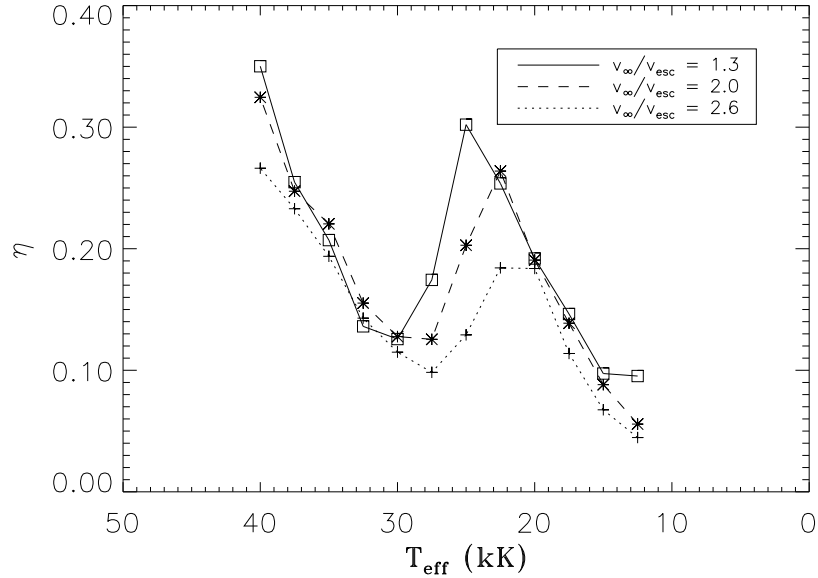


**Fig. 4.** The wind efficiency number  $\eta = \dot{M}v_\infty/(L_*/c)$  as a function of  $T_{\text{eff}}$  for three values of the ratio  $v_\infty/v_{\text{esc}}$ . These values are indicated in the upper right corner. Note the steady decrease of  $\eta$  to lower temperatures, except the jump of about a factor 2 or 3 near 25 000 K.

jump by a factor of about five, which was already shown in the lower panel of Fig. 3.

The behaviour of  $\eta$  as a function of  $T_{\text{eff}}$  is not exactly the same for the three different series of models. First, the size of the jump is different. Second, the jump occurs at somewhat different temperatures. This is no surprise, since the ionization equilibrium does not only depend on  $T$ , but on  $\rho$  as well, a smaller value of the velocity  $v_\infty$ , means a larger density  $\rho$  in the wind. Hence, the jump is expected to start at a larger value of  $T_{\text{eff}}$  for a smaller value of  $v_\infty/v_{\text{esc}}$ . This behaviour for the position of  $T_{\text{eff}}$  of the jump can be seen in  $\dot{M}$  in Fig. 3 and in  $\eta$  in Fig. 4.

## 6. The origin of the bi-stability jump

In the previous section we have shown that the mass-loss rate increases around  $T_{\text{eff}} = 25 000$  K. The next step is to investigate the physical process that causes the bi-stability jump. Therefore, we will look into the details of the line acceleration  $g_L(r)$  for three models around the bi-stability jump. For these models (A, B and C in Table 1 and Fig. 3) we made improved Monte-Carlo calculations, using  $2 \times 10^7$  packets of photons, to derive more details about the radiative acceleration.

First, we will investigate the line acceleration  $g_L(r)$  of the model at the hot side of the bi-stability jump. This model A with  $T_{\text{eff}} = 27 500$  K and  $v_\infty/v_{\text{esc}} = 2.6$ , is our basic model. Then, we will compare model A to model B that has the same  $v_\infty/v_{\text{esc}}$ , but is situated on the cool side of the bistability jump, where  $T_{\text{eff}} = 25 000$  K. By comparing models A and B, we can investigate the intrinsic

increase in  $\dot{M}$  of 45 % in our model calculations due to the lower  $T_{\text{eff}}$ . The next step is to compare  $g_L(r)$  of model B and model C which also has  $T_{\text{eff}} = 25 000$  K, but a smaller ratio  $v_\infty/v_{\text{esc}} = 1.3$ . By comparing model B and C, we can obtain information about the effects of a jump in  $v_\infty$ . Finally, we check our approach for self-consistency by simultaneously calculating the mass-loss rate and terminal velocity.

### 6.1. The main contributors to the line acceleration

Model A has a mass-loss rate of  $\log \dot{M} = -6.95$ . The behaviour of the line acceleration as a function of the distance from the stellar surface,  $g_L(r)$  is shown in Fig. 5. The sonic point is reached at a distance of  $1.025 R_*$ . It is clear that most of the line driving is produced far beyond the sonic point. But, as was explained in Sect. 2 the important region that determines the mass-loss rate is *below* the sonic point. Therefore, the part of the atmosphere around the sonic point is enlarged in Fig. 5(b).

To investigate the origin of the jump, it is useful to know which elements are effective line drivers in which part of the stellar wind. Therefore, extra Monte-Carlo calculations were performed. The first extra Monte-Carlo simulation was performed with a line list containing only Fe lines. The second one was performed with a line list containing the lines of the elements C, N and O.

Figure 5(b) shows that Fe is the main line driver below the sonic point. C, N and O, are important line drivers in the supersonic part of the wind, which can be seen in 5(a).

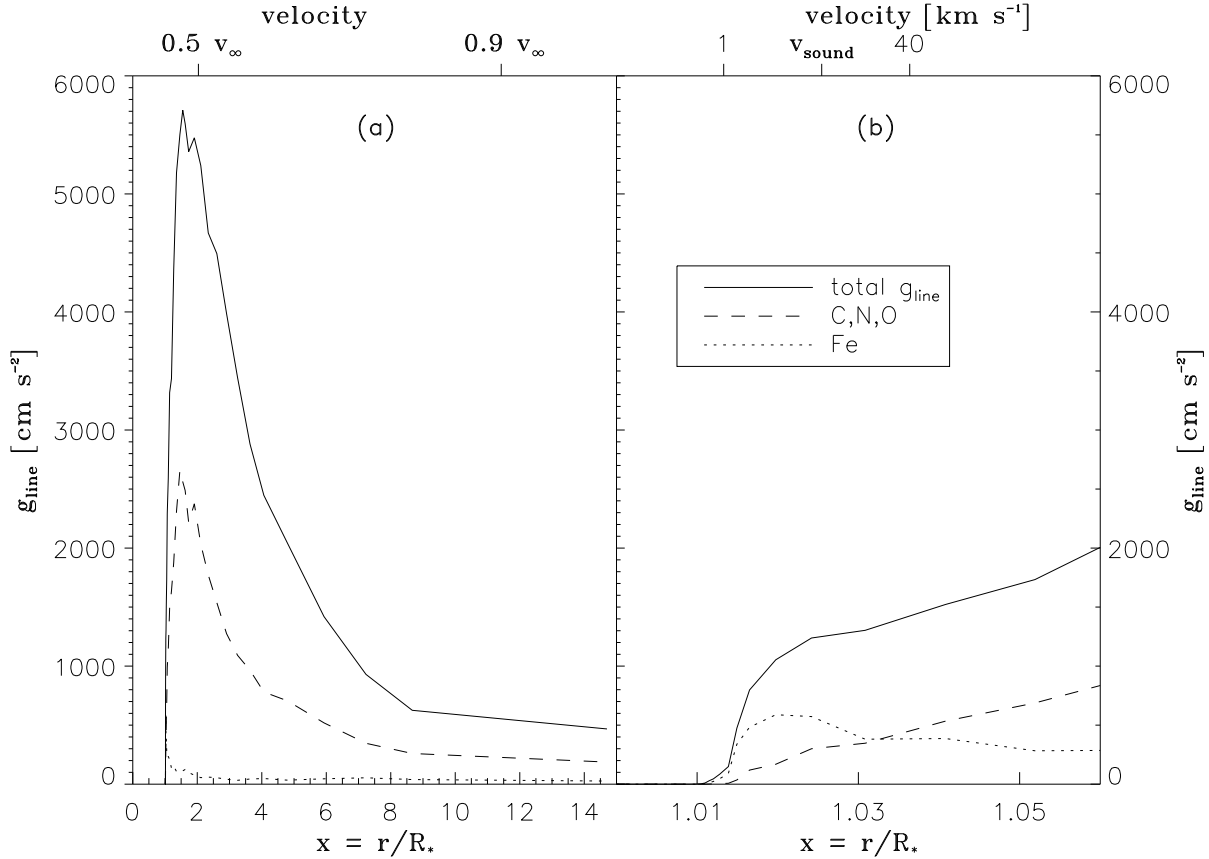


**Fig. 5.** The line acceleration of model A ( $T_{\text{eff}} = 27\,500$  K and  $v_{\infty}/v_{\text{esc}} = 2.6$ ), from 1 to  $15 R_*$  (left) and around the sonic point (right). (a) The solid line shows the total  $g_L$  as a function of the distance. The dashed line is the contribution by C, N and O only. The dotted line shows the contribution by Fe lines. Some values for the velocity are indicated on top of the figure. (b) The region around the sonic point is enlarged. The sonic point is reached at  $x = 1.025$ . Note the bump in the  $g_L(r)$  just below the sonic point, which is largely due to Fe lines.

C, N and O contribute roughly 50 % of the line acceleration in the supersonic part of the wind. Not indicated here, but relevant to mention is that Si, Cl, P and S are other important line drivers in the supersonic part of the wind. Ni was found *not* to be an important line driver in any part of the stellar wind at all.

The mass-loss rate is determined by the radiative acceleration *below* the sonic point, and the terminal velocity is determined by the radiative acceleration in the *supersonic* part of the wind. So our results show that the mass-loss rates of hot star winds are mainly determined by the radiation pressure due to Fe! The terminal velocities are mainly determined by the contributions of C, N and O.

## 6.2. The effect of the Fe ionization

To understand the origin of the bi-stability jump in  $\dot{M}$ , we investigate the line acceleration due to Fe. The ionization balance of Fe for models A and B is plotted in Fig. 6, top and bottom respectively. The right hand figures show the enlargement of the ionization balance in the region near

the sonic point. In Model A ( $T_{\text{eff}} = 27\,500$  K) Fe V has a maximum around  $x = 1.004$ , which can be seen in Fig. 6 (b). Then, due to the outward decreasing temperature, Fe V decreases in favour of Fe IV, which peaks around  $x = 1.008$ . Next, one may expect Fe IV to decrease in favour of Fe III. However, around  $x = 1.013$  Fe IV reionizes due to a decrease of the density  $\rho$ . In this region of the atmosphere, where  $dv/dr$  is rapidly increasing, the effect of the decreasing  $\rho$  is larger than the effect of the decreasing  $T$ .

Fig. 6 (b) clearly shows that Fe IV is the dominant ionization stage in the subsonic region of the stellar wind. In the region just below the sonic point, the ionization fraction of Fe IV is 90 - 100 % whereas that of Fe III is less than 10 %. However, this does not necessarily mean that Fe IV is the main line driver. To investigate the contribution to the line acceleration  $g_L$  of the different ionization stages of Fe some extra Monte-Carlo simulations were performed. One simulation included only the lines of Fe III, another simulation included just the lines of Fe IV. The results for  $g_L$  for Fe III and Fe IV are plotted in Fig. 7.

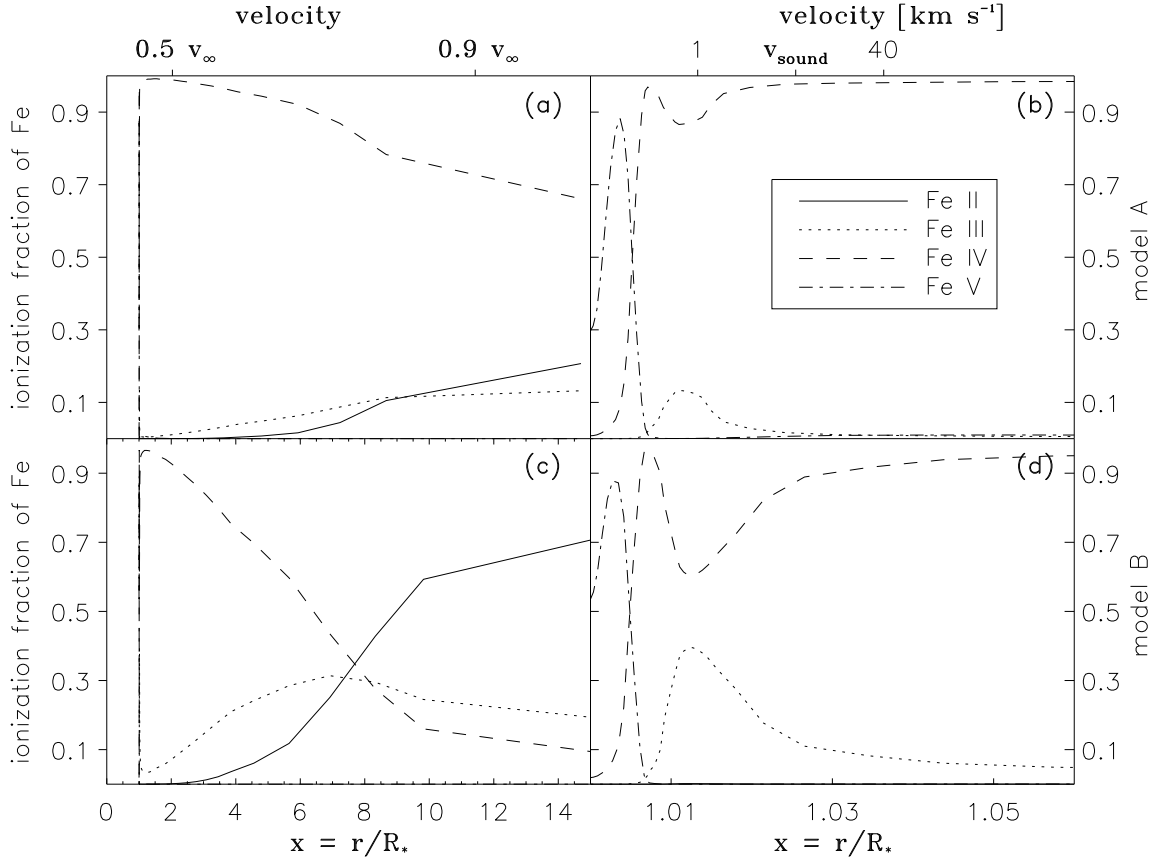


**Fig. 6.** The ionization fraction of Fe as a function of distance. The upper panels are for model A and the lower panels for model B. (a) Fe ionization for model A from  $x = 1$  to 15. (b) Model A, enlarged around sonic point. (c) Fe ionization for model B from  $x = 1$  to 15. (d) Model B, enlarged around sonic point.

It is surprising to note that, although Fe IV is the dominant ionization stage throughout the wind, most of the driving is contributed by Fe III. Below the sonic point Fe III is clearly the most important iron line driver (see Fig. 7(b)).

From the data shown in Figures 6 and 7 we conclude that the mass-loss rate of winds from stars with  $T_{\text{eff}} \simeq 27\,500$  K is mainly determined by the radiative acceleration due to Fe III lines. This suggests that the bi-stability jump is mainly due to changes in the ionization balance of Fe. We test this hypothesis in the next section.

### 6.3. The effect of $T_{\text{eff}}$ on $\dot{M}$

In the previous section we have shown that the mass loss of model A is dominated by radiative acceleration due to Fe III lines. In this section we investigate changes in the radiative acceleration due to Fe as  $T_{\text{eff}}$  decreases. This may explain the increase of  $\dot{M}$  near the bi-stability jump. To this purpose we compare the ionization and  $g_L$  of models A and B in detail.

The ionization balance of model B is shown in Fig. 6(c) and (d). It shows that, due to a lower temperature, the

decrease of the Fe IV fraction drops to smaller values than for model A, which was shown in Fig. 6(b). The ionization fraction of Fe III below the sonic point in the case of model B is up to almost 40 %. To see whether this extra amount of Fe III can cause the increase in the line acceleration, we must look at  $g_L$  of Fe for model B.

Since model A and B have different  $T_{\text{eff}}$  at the same  $L_*$ , they have a different radiative surface flux. The radiative acceleration will be proportional to this flux. In order to compare the values of  $g_L$  of the two models, we scale the results to a flux of a  $T_{\text{eff}} = 25\,000$  K model. So

$$g_L^{\text{norm}} = g_L \left( \frac{25000}{T_{\text{eff}}} \right)^4 \quad (36)$$

Since  $T_{\text{eff}}^4 \propto R_*^{-2}$  for constant luminosity, this is also a scaling to the Newtonian gravity of the models.

Figure 8 shows the normalized  $g_L$  of Fe for the models A (top) and B (bottom). The right hand figures show an enlargement of the region near the sonic point. It shows that for model B  $g_L$  of Fe III around the sonic point is more than a factor two larger than for model A (see Figs. 8(b) and (d)). This extra amount of Fe III in model B causes

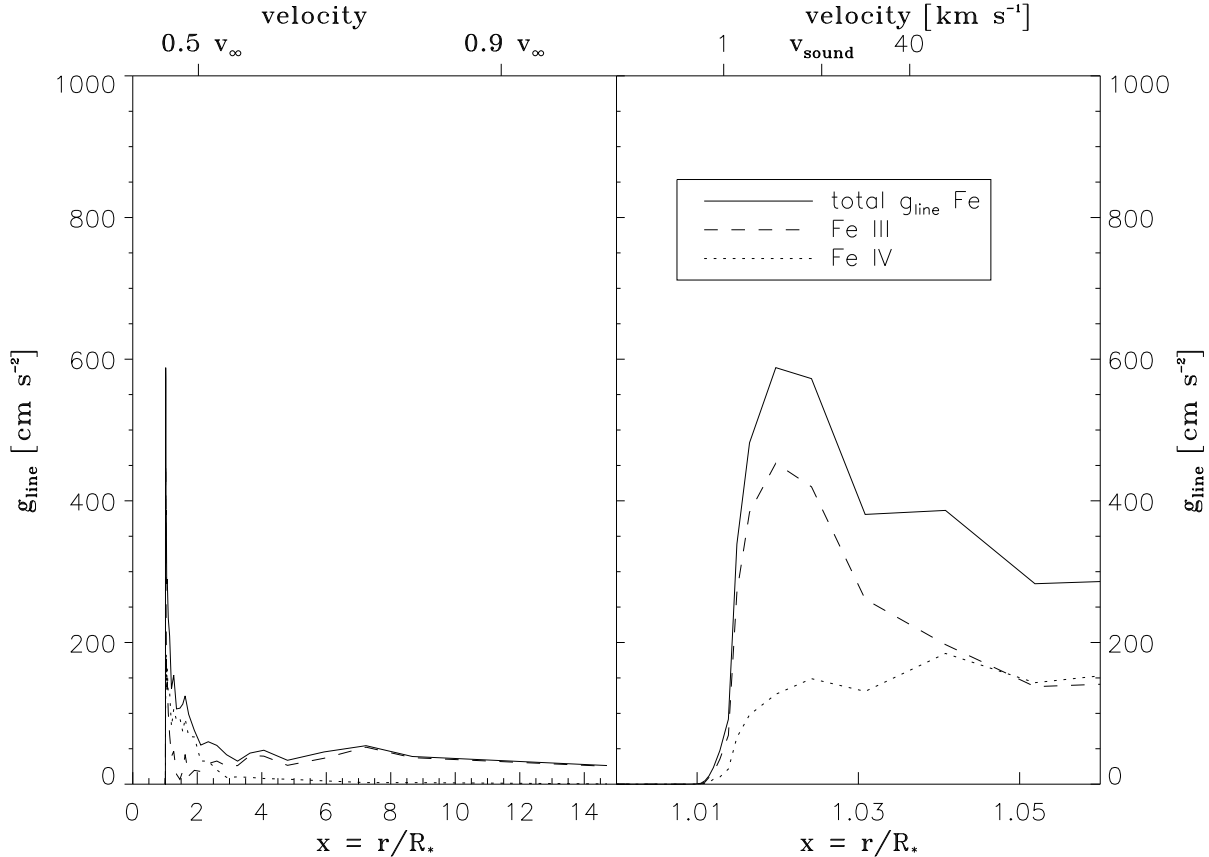


**Fig. 7.** The contribution of several Fe ions to  $g_L$  as a function of distance from the stellar surface for model A. (a) The full distance range of  $x = 1$  to 15. (b) The region around the sonic point is enlarged. The legend indicates the ionization stage. Some values for the velocity are indicated on the top of the figure. Note that the strongest contribution to  $g_L$  below the sonic point is due to Fe III, although the ionization fraction of this ion is less than 10 %.

an increase in the *total*  $g_L$  in the subsonic part of the wind also, as can be seen in Fig. 9(b).

We conclude that the increase in mass loss from model A to B is due to the larger radiative acceleration (compared to the gravity) of model B by a larger ionization fraction of Fe III below the sonic point.

#### 6.4. The effect of $v_\infty$

Now the effect of  $g_L$  on  $v_\infty$  will be examined. Therefore, Model B is compared to model C. We remind that models B and C have the same  $T_{\text{eff}}$ , and hence the same radiative flux and gravity, but model C has a twice as small value of  $v_\infty/v_{\text{esc}}$  as model B. Figure 9(a) shows the normalized  $g_L$  for models A, B and C. As expected,  $g_L(r)$  for model C is significantly smaller than  $g_L(r)$  for models A and B. This is obviously due to the smaller value of  $v_\infty$ . The integral  $\int g_L(r) dr$  in Fig. 9(a) for model A and B is larger than for model C. The values of  $\int g_L(r) dr$  for the models are  $2.34 \times 10^{16}$  and  $1.92 \times 10^{16} \text{ cm}^2 \text{ s}^{-2}$  for models A and B respectively, and  $6.12 \times 10^{15} \text{ cm}^2 \text{ s}^{-2}$  for model C. Using Eq. 7 and the values of  $v_{\text{esc}}$  from column (4) in Table 1, the output values for  $v_\infty$  can be obtained from the val-

ues of the integral of  $g_L$ . The derived output values for  $v_\infty$  for the models are  $v_\infty = 2050, 1860$  and  $920 \text{ km s}^{-1}$  respectively for the models A, B and C. These values are equal within 10 % to the input values for  $v_\infty$  which were indicated in column (5) of Table 1. We can conclude that a smaller value for  $v_\infty$  is indeed consistent with a smaller value of the integral  $\int g_L(r) dr$ . However, this is not an independent check, since the calculated line acceleration of optically thick lines (in the Sobolev approximation) is inversely proportional to the Sobolev optical depth which is proportional to  $(dv/dr)^{-1}$ . Hence, *assuming* a smaller terminal velocity will automatically result in a smaller calculated line acceleration.

#### 6.5. A self-consistent solution of the momentum equation

In earlier sections we have demonstrated that the mass loss around the bi-stability jump increases. As we have used *observed* values for the ratio  $v_\infty/v_{\text{esc}}$  in our model calculations, we have not yet provided a self-consistent explanation of the observed bi-stability jump in  $v_\infty/v_{\text{esc}}$ . As a consistency test of our calculations and an attempt to explain the observed jump in the ratio  $v_\infty/v_{\text{esc}}$ , we

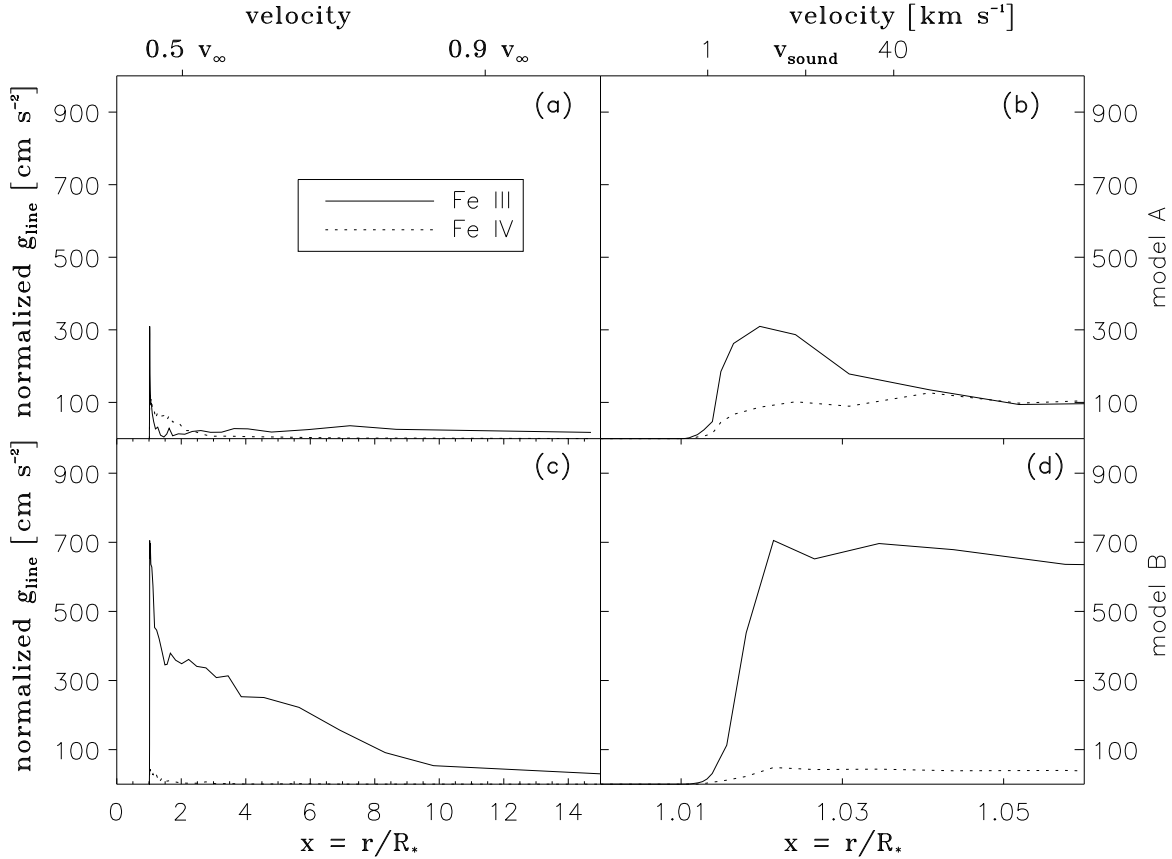


**Fig. 8.** Normalized  $g_L$  of Fe as a function of distance from the stellar surface for the models A and B. (a) Normalized  $g_L$  for the different Fe ionization stages of model A. The legend indicates the ionization stage. Some values for the velocity are indicated on the top of the figure. (b) model A, enlarged around the sonic point. (c) Normalized  $g_L$  for the different Fe ionization stages of model B. (d) model B, enlarged around sonic point.

**Table 2.** Force multipliers and consistent models.

$\log L/L_\odot = 5.0$ ,  $M = 20M_\odot$ ,  $\Gamma_e = 0.130$ ,  $M_{\text{eff}} = 17.4 M_\odot$ ,  $\beta = 1$ , solar metallicity.

$T_{\text{eff}}$ (K)	$(v_\infty/v_{\text{esc}})_0$	$(v_\infty/v_{\text{esc}})_1$	$(v_\infty/v_{\text{esc}})_2$	$(v_\infty/v_{\text{esc}})_3$	$\alpha^{\text{MC}}$	$k^{\text{MC}}$	$(v_\infty/v_{\text{esc}})_4$	$\log \dot{M}_{\text{CAK}}$ ( $M_\odot/\text{yr}$ )	$\log \dot{M}_{\text{MC}}$ ( $M_\odot/\text{yr}$ )
17 500	2.0	1.5	1.3	1.2	0.58	0.2065	1.2	-6.21	-6.27
30 000	2.0	2.5	2.4	2.4	0.85	0.0076	2.4	-6.86	-6.90

proceeded to solve the momentum equation of line driven wind models around the bi-stability jump. The approach we take is to combine predicted force multiplier parameters  $k$  and  $\alpha$  (see below) from the Monte Carlo calculation with the analytical solution of line driven winds from CAK.

We calculated the line acceleration  $g_L$  for several models with different  $T_{\text{eff}}$  using the Monte Carlo method. The values of  $g_L$  were expressed in terms of the force multiplier  $M(t)$  (Eq. 8). Following CAK we tried to express  $M(t)$  in terms of a power-law fit of the optical depth parameter  $t$  (Eq. 9). We found that in the range  $20\,000 \leq T_{\text{eff}} \leq 27\,500$ ,  $M(t)$  is not accurately fit by a power-law, since the ionization changes over this critical range in  $T_{\text{eff}}$ . For-

tunately, just outside this temperature region,  $M(t)$  can be accurately represented in terms of  $k$  and  $\alpha$ , i.e.

$$M^{\text{MC}}(t) = k^{\text{MC}} t^{-\alpha^{\text{MC}}} \quad (37)$$

Therefore, we have calculated models with effective temperatures just below ( $T_{\text{eff}} = 17\,500$  K) and just above ( $T_{\text{eff}} = 30\,000$  K) this critical temperature range. Self-consistent values of  $v_\infty$  and  $\dot{M}$  were thus found in the following way:

1. We started with an assumed ratio of  $v_\infty/v_{\text{esc}} = 2.0$  (See column (2) in Table 2).
2. The force multipliers  $M^{\text{MC}}(t)$  were calculated and a power-law fit of the type Eq. 37 was derived. The fit

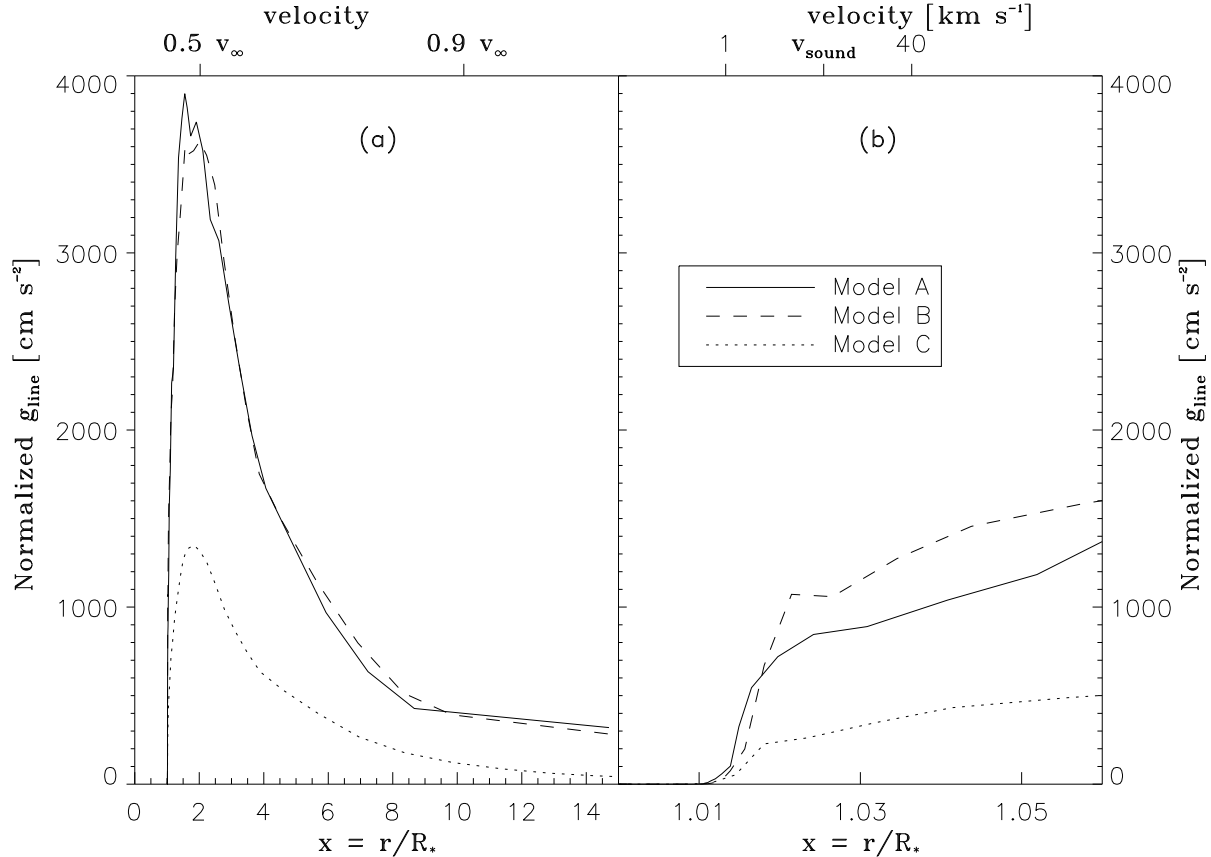


**Fig. 9.** (a) The normalized *total*  $g_L$  for the models A, B and C as a function of distance. Notice the much smaller radiative acceleration in the supersonic region of model C compared to models A and B. (b) An enlargement of the region around the sonic point. The sonic point is located around  $x = 1.025 r/R_*$ . Notice also the much smaller radiative acceleration in the subsonic region of model C compared to models A and B. This is due to the smaller value of  $v_\infty/v_{\text{esc}}$  for model C.

was found to be excellent in the important part of the wind between the sonic point and  $v \simeq 0.5v_\infty$ . This yielded values of  $\alpha^{\text{MC}}$  and  $k^{\text{MC}}$ . Next, the mass loss and terminal velocity were simultaneously calculated from these  $\alpha^{\text{MC}}$  and  $k^{\text{MC}}$  parameters using the CAK solution of the momentum equation. Note that the solution with the finite disk correction (Pauldrach et al. 1986) was *not* applied, since this is already properly taken into account in the values of  $\alpha^{\text{MC}}$  and  $k^{\text{MC}}$  calculated in the Monte Carlo technique (see Sect. 3). The superscript, MC, to the force multiplier parameters was added to avoid confusion with  $k$  and  $\alpha$  for a point-like source used by e.g. Kudritzki et al. (1989). The ratio  $v_\infty/v_{\text{esc}}$  can be derived from the simple CAK formulation:

$$\frac{v_\infty}{v_{\text{esc}}} = \sqrt{\frac{\alpha^{\text{MC}}}{1 - \alpha^{\text{MC}}}} \quad (38)$$

The value for  $\alpha^{\text{MC}}$  for the model of 30,000 K is significantly higher than values for  $\alpha$  that were calculated

before (e.g. Pauldrach et al. 1986), since the finite disk is already included in the  $\alpha^{\text{MC}}$ -parameter!

3. The new calculated terminal velocity ratio  $v_\infty/v_{\text{esc}}$  (column (3) of Table 2) was used in the next iteration.
4. New mass-loss rates were calculated from the MC approach using the procedure as explained in Sect. 3.4. The mass-loss rates are equal within 15 % to the mass-loss rates that can be calculated using the expression for  $\dot{M}$  of CAK using  $\alpha^{\text{MC}}$  and  $k^{\text{MC}}$ .
5. The above procedure (step 1. through 4.) was repeated until convergence was reached. After four iterations, the ratio  $v_\infty/v_{\text{esc}}$  did not change anymore. The intermediate values of  $v_\infty/v_{\text{esc}}$  are given in columns (3), (4) and (5) of Table 2. The final value for the ratio  $v_\infty/v_{\text{esc}}$  is given in column (8). For the hot model ( $T_{\text{eff}} = 30\,000$  K) the final ratio  $v_\infty/v_{\text{esc}}$  equals 2.4; for the cool model ( $T_{\text{eff}} = 17\,500$  K)  $v_\infty/v_{\text{esc}} = 1.2$ . These values are within 10 % of the observed values of  $v_\infty/v_{\text{esc}}$ , i.e. 2.6 and 1.3 respectively.
6. CAK mass-loss rates were also calculated from the resulting *final* force multiplier parameters  $k^{\text{MC}}$  and  $\alpha^{\text{MC}}$

(given in columns (6) and (7) of Table 2 and the *final* mass-loss rates are given in column (9) of this Table. Note that the values of  $\dot{M}$  are only marginally different from the mass-loss rates that were calculated from the Monte Carlo approach (column (10) of Table 2).

In summary; we have self-consistently calculated values of  $v_\infty$  and  $\dot{M}$  of two models located at either side of the bi-stability jump. We have found a jump in terminal velocity  $v_\infty/v_{\text{esc}}$  of a factor of two, similar as observed by Lamers et al. (1995). Moreover, the mass-loss rates calculated from the CAK formulation are consistent with those obtained from our Monte Carlo approach. *This implies that the origin of the observed change in the ratio  $v_\infty/v_{\text{esc}}$  of a factor of two around spectral type B1 is identical to the predicted jump in mass-loss rate of a factor of five due to the recombination of Fe IV to Fe III.*

#### 6.6. Conclusion about the origin of the bi-stability jump

From the results and figures presented above we conclude that the mass-loss rate of early-B supergiants near the bi-stability jump is mainly determined by the radiative acceleration by iron. Although Fe IV is the dominant ionization stage in the atmosphere of stars near 25 000 K, it is Fe III that gives the largest contribution to the subsonic line acceleration. This is due to the number of effective scattering lines and their distribution in wavelengths, compared to the energy distribution from the photosphere. This implies that the mass-loss rates of B-supergiants are very sensitive to the ionization equilibrium of Fe in the upper photosphere. Our models show that the ionization fraction of Fe III increases drastically between  $T_{\text{eff}} = 27\,500$  and 25 000 K. This causes an increase in the line acceleration below the sonic point and in turn increases the mass loss near the bi-stability jump.

### 7. Bi-stability and the variability of LBV stars

Luminous Blue Variables (Conti 1984) are massive stars undergoing a brief, but important stage of evolution. During this period they suffer severe mass loss with  $\dot{M}$  values of up to  $10^{-4}M_\odot\text{yr}^{-1}$ . LBVs are characterized by typical variations in the order of  $\Delta V$  of 1 to 2 magnitudes. Nevertheless, the total bolometric luminosity of the star  $L_*$  seems to be about constant. The reason for the typical LBV variations is still unknown. For reviews see Nota & Lamers (1997).

Leitherer et al. (1989) and de Koter et al. (1996) have shown that it must be the actual radius of the star that increases during these typical variations. Therefore,  $T_{\text{eff}}$  decreases during the variations, if  $L_*$  is about constant. In this paper, we have calculated the mass-loss behaviour for normal OB supergiants as a function of  $T_{\text{eff}}$ . Despite many differences between OB supergiants and LBVs, we can retrieve valuable information about the behaviour of

$\dot{M}$  during a typical LBV variation by investigating the  $\dot{M}$  behaviour of normal OB supergiants, since both types of stars are located in the same part of the HRD. Our calculations can be used as a tool to understand the mass loss changes of an LBV in terms of changes in  $T_{\text{eff}}$  during such a typical variation (see also Leitherer et al. 1989).

Observations of LBVs show that for some LBVs that undergo typical variations  $\dot{M}$  is increasing from visual minimum to maximum, while for others it is the other way around:  $\dot{M}$  is decreasing. This “unpredictable” behaviour of  $\dot{M}$  during an LBV variation is not a complete surprise, if one considers our  $\dot{M}$  values as a function of  $T_{\text{eff}}$ . We have found that in the ranges  $T_{\text{eff}} = 40\,000\text{--}30\,000$  K and  $T_{\text{eff}} = 20\,000\text{--}12\,500$  K,  $\dot{M}$  decreases for a decreasing  $T_{\text{eff}}$ , whereas in the interval between  $T_{\text{eff}} = 30\,000\text{--}20\,000$  K,  $\dot{M}$  increases for a decreasing  $T_{\text{eff}}$ . This shows that whether one expects an increasing or decreasing  $\dot{M}$  during an LBV variation depends on the specific range in  $T_{\text{eff}}$  between visual minimum and maximum. This was already suggested by Lamers (1997), albeit a constant value of  $\eta$  was anticipated.

Our present calculations cannot be used to model the observed LBV variations, because we have assumed solar metallicities, whereas the LBVs are known to have an enhanced He and N abundance (e.g. Smith et al. 1994). Moreover, since most LBVs have already suffered severe mass loss in the past, their  $L_*/M_*$  ratio will be higher than for normal OB supergiants. This means that LBVs are closer to their Eddington limit, which one may expect to have an effect on  $\dot{M}$  also. These combined effects explain the lack of a consistent behaviour of  $\dot{M}$  for LBV variations so far. Especially since it is not sure that  $L_*$  really remains constant during the variations (see Lamers 1995).

### 8. Summary, Discussion, Conclusions & Future work

We have investigated the nature of the observed jump in the ratio  $v_\infty/v_{\text{esc}}$  of the winds of supergiants near spectral type B1.

Calculations for wind models of OB supergiants show that around  $T_{\text{eff}} = 25\,000$  K the mass-loss rate  $\dot{M}$  jumps due to an increase in the line acceleration of Fe III below the sonic point. This jump in  $\dot{M}$  is found in three different series of models. In all cases, the wind efficiency number  $\eta = \dot{M}v_\infty/(L_*/c)$  increases significantly, by about a factor of 2 to 3, if  $T_{\text{eff}}$  decreases from about 27 500 K to about 22 500 K. Observations show that the ratio  $v_\infty/v_{\text{esc}}$  drops by a factor of two around spectral type B1. Applying these values for  $v_\infty/v_{\text{esc}}$ , we predict a bi-stability jump in  $\dot{M}$  of about a factor of five. So  $\dot{M}$  is expected to increase by about this factor between 27 500 and 22 500 K.

We have argued that the mass loss is determined by the radiative acceleration in the subsonic part of the wind, i.e. below  $r \simeq 1.03R_*$ . We found that this radiative accel-

eration is dominated by the contribution of the Fe III lines. Therefore  $\dot{M}$  is very sensitive to both the metal abundance and to the ionization equilibrium of Fe. Our models show that the ionization fraction of Fe III and the subsonic radiative acceleration increases steeply between  $T_{\text{eff}} = 27\,500$  and  $25\,000$  K. This explains the calculated increase in  $\dot{M}$  in this narrow temperature range.

The exact temperature of the bi-stability jump is somewhat ambiguous. Observations indicate that the jump occurs around spectral type B1, corresponding to  $T_{\text{eff}} \simeq 21\,000$  K (Lamers et al. 1995). If one would not completely trust the value of  $v_{\infty}/v_{\text{esc}}$  for the star HD 109867 (number 91 in Lamers et al. (1995)), because of its relatively large error bar, then  $T_{\text{eff}}$  of the observed jump can easily occur at a few kK higher. In fact we cannot expect the bi-stability jump to occur at one and the same temperature for all luminosity classes, because the jump is sensitive to the ionization balance (mainly of Fe III) in the subsonic region of the wind and hence to the gravity of the star. Our models predict that the jump will occur near  $T_{\text{eff}} \simeq 25\,000$  K. However, this is sensitive to the assumptions of the models: the adopted masses and luminosities and to the assumption of the modified nebular approximation for the calculation of the ionization equilibrium of iron (see Sect. 4).

A more consistent treatment of the ionization and excitation equilibrium of the Fe-group elements may have two effects: *i*)  $\dot{M}$  predicted from  $\Delta L$  may alter, and *ii*)  $T_{\text{eff}}$  at which the ionization ratio of e.g. Fe III/IV flips, may shift. Nevertheless, in view of the very encouraging results using the modified nebular approximation in the modeling of UV metal-line forests (de Koter et al. 1998), we expect the error in  $T_{\text{eff}}$  at which the dominant ionization of Fe switches from IV to III to be at most a few kK. Furthermore, if a more consistent treatment would yield a change in  $\dot{M}$  this would most likely produce a systematic shift. Since we are essentially interested in relative shifts in  $\dot{M}$ , we do not expect that our conclusions regarding the nature of the bi-stability jump would be affected.

It is relevant to mention that Leitherer et al. (1989) calculated atmospheric models for LBVs and suggested that the recombination of iron group elements from doubly to singly ionized stages, which according to them, occurs around  $T_{\text{eff}} = 10\,000$  K, can explain  $\dot{M}$  increases when LBVs approach their maximum states. We have found a Fe III/IV ionization/recombination effect around  $T_{\text{eff}} = 25\,000$  K for normal supergiants. We also anticipate that somewhere, at a lower value of  $T_{\text{eff}}$  a similar ionization/recombination effect will occur for Fe II/III, causing a *second* bi-stability jump. Lamers et al. (1995) already mentioned the possible existence of a second bi-stability jump around  $T_{\text{eff}} = 10\,000$  K from their determinations of  $v_{\infty}/v_{\text{esc}}$ , but the observational evidence for this second jump was meagre. Possibly, this second jump *is* real and we anticipate that this second jump could very well originate from a Fe II/III ionization/recombination effect.

Furthermore, we have shown that the elements C, N and O are important line drivers in the *supersonic* part of the wind, whereas the *subsonic* part of the wind is dominated by the line acceleration due to Fe.<sup>1</sup> Therefore, we do *not* expect CNO-processing to have a large impact on  $\dot{M}$ , but it might have impact on the terminal velocities.

Finally, we would like to add that our calculations for  $\dot{M}$  around  $T_{\text{eff}} = 25\,000$  K have only been performed for *one* value of  $M_*$ ,  $L_*$  and H/He abundance.  $\dot{M}$  is expected to depend on these stellar parameters, so calculating mass-loss rates for a wider range of stellar parameters will provide valuable information on the size of the bi-stability jump in  $v_{\infty}$  and  $\dot{M}$  and will allow us to constrain its amplitude and location in the HRD.

*Acknowledgements.* We thank an anonymous referee for several useful suggestions. JV acknowledges support from the Netherlands Foundation for Research in Astronomy (NFRA) with financial aid from the Netherlands Organization for Scientific Research (NWO). AdK acknowledges support from a NWO "Pionier" grant to L.B.F.M. Waters; from NWO Spinoza grant 08-0 to E.P.J. van den Heuvel and from a grant from the NASA Astrophysics Data Program NRA 95-ADP-09 to S.R. Heap.

## References

Abbott D.C., 1982, ApJ 259, 282  
 Abbott D.C., Lucy L.B., 1985, ApJ 288, 679  
 Castor J.I., Abbott D.C., Klein R.I., 1975, ApJ 195, 157  
 Conti P.S., 1984, in: Maeder A., Renzini A. (eds.) Proc. IAU Symp. 105, Observational Tests of Stellar Evolution Theory, Kluwer, Dordrecht, p. 233  
 de Koter A., Schmutz W., Lamers H.J.G.L.M., 1993, AAP 277, 561  
 de Koter A., Lamers H.J.G.L.M., Schmutz W., 1996, A&A 306, 501  
 de Koter A., Heap S.R., Hubeny I., 1997, ApJ 477, 792  
 de Koter A., Heap S.R., Hubeny I., 1998, ApJ 509, 879  
 Drew J.E., 1989, ApJS 71, 267  
 Groenewegen M.A.T., Lamers H.J.G.L.M., 1989, A&AS 79, 359  
 Kudritzki R.-P., Pauldrach A.W.A., Puls J., Abbott D.C., 1989, AAP 219, 205  
 Kurucz R.L., 1988, IAU Trans., 20b, 168  
 Lamers H.J.G.L.M., 1995, in: Astrophysical Applications of Stellar Pulsations, ASP Conf.Ser. 83, 176  
 Lamers H.J.G.L.M., 1997, in: Luminous Blue Variables: Massive Stars in Transition, ASP Conf.Ser. 120, 76  
 Lamers H.J.G.L.M., Cassinelli J.P., 1999, in: Introduction to Stellar Winds, Cambridge Univ. Press, Chapter 3  
 Lamers H.J.G.L.M., Pauldrach A.W.A., 1991, A&A 244, L5  
 Lamers H.J.G.L.M., Snow T.P., Lindholm D.M., 1995, ApJ 455, 269

<sup>1</sup> When this study was finished we received a preprint by Puls et al. (1999) who have independently found that the Fe-group elements control the line acceleration in the inner wind part, whereas light ions dominate the outer part.

Lamers H.J.G.L.M., Vink J.S., de Koter A., Cassinelli J.P., 1999, in: Variable and Non-Spherical Stellar Winds in Luminous Hot Stars, 159

Leitherer C., Schmutz W., Abbott D.C., Hamann W.R., Wesolowski U., 1989, ApJ 346, 919

Lucy L.B., 1998, in: Cyclical Variability in Stellar Winds, ESO ASS Proc 22, 16

Lucy L.B., Abbott D.C., 1993, ApJ 405, 738

Mazzali P.A., Lucy L.B., 1993, A&A 279, 447

Nota A., Lamers H.J.G.L.M., 1997, Luminous Blue Variables: Massive Stars in Transition, ASP Conf.Ser. 83.

Pauldrach A.W.A., Puls J., 1990, A&A 237, 409

Pauldrach A.W.A., Puls J., Kudritzki, R.P., 1986, A&A 164, 86

Puls J., Kudritzki R.P., Herrero A., et al., 1996, A&A 305, 171

Puls J., Springmann U., Lennon, M, A&A submitted

Schmutz W., 1991. In: Stellar Atmospheres: Beyond Classical Models, eds. Crivellari L., Hubeny I., Hummer D.G., NATO ASI Series C, Vol. 341, 191

Schmutz W., Abbott D.C., Russell R.S., Hamann W.-R., Wesolowski U., 1990, ApJ 355, 255

Smith L.J., Crowther P.A., Prinja R.K., 1994, A&A 281, 833